

Soft x-ray resonant magneto-optical constants at the Gd $M_{4,5}$ and Fe $L_{2,3}$ edgesJ. F. Peters,* J. Miguel, M. A de Vries,[†] O. M. Toulemonde,[‡] and J. B. Goedkoop[§]*Van der Waals-Zeeman Institute, University of Amsterdam, Valckenierstraat 65, 1018 XE, Amsterdam, The Netherlands*S. S. Dhesi^{||} and N. B. Brookes*European Synchrotron Radiation Facility, ESRF, BP 220, F-38043 Grenoble Cedex, France*

(Received 18 November 2003; revised manuscript received 18 June 2004; published 15 December 2004)

We present absolute values for the complete set of magneto-optical constants around the Gd_{4,5} and Fe $L_{2,3}$ dipole resonances as obtained from measurement of the polarization dependent photoabsorption cross sections and Kramers-Kronig transformation. The results are verified by comparing the resulting resonant scattering factors with the resonant magnetic scattering from a stripe domain lattice, showing an excellent agreement for both the circular and linear dichroic contributions.

DOI: 10.1103/PhysRevB.70.224417

PACS number(s): 71.20.Eh, 78.20.Ls, 78.70.Dm

I. INTRODUCTION

The large magneto-optical effects around the x-ray core level resonances that were discovered in the eighties¹⁻⁷ have become an indispensable tool in modern magnetism research.⁸⁻²¹ While polarization dependent x-ray absorption is a powerful probe of element-specific magnetization,^{4-18,21} the magneto-optical contrast can also be used to resolve the magnetic structure in resonant magnetic scattering^{2,3,18,22-27} and microscopy^{11-15,28,29} experiments. Scattering experiments are most readily performed using hard x rays ($\hbar\omega > 2$ keV), which have the combined advantage of high spatial resolution and large penetration power.^{2,3} However, in the soft x-ray range the resonant magnetic scattering cross sections are much larger and although unfortunately the soft x-ray wavelengths (~ 1 nm) are too large for the determination of the unit cell structure, they are perfectly suited to resolve the micromagnetic structure of domains and the artificial structures as multilayers and nanostructured devices. The early soft x-ray magnetic scattering experiments concentrated on reflectivity measurements at the transition metal $L_{2,3}$ edges on single crystal surfaces²² and magnetic multilayers²³⁻²⁵ and showed the possibility of obtaining magnetization profiles near the interfaces. More recently the technique was applied to the study of the domain structure of thin films, both in reflectivity²⁶ and transmission^{27,30} geometries, and concentrated on FePd and CoPt thin films, multilayers and patterned surfaces.³¹

For the interpretation of resonant scattering experiments, quantitative knowledge of the polarization and energy dependent magneto-optical constants is essential. For dipole resonances, as discussed here, the resonant contribution f_{E1} to the atomic scattering amplitude f is given by^{3,32}

$$f_{E1}(\hat{\mathbf{e}}, \hat{\mathbf{e}}') = (\hat{\mathbf{e}}'^* \cdot \hat{\mathbf{e}})F^{(0)} - i(\hat{\mathbf{e}}'^* \times \hat{\mathbf{e}}) \cdot \mathbf{m}F^{(1)} + (\hat{\mathbf{e}}'^* \cdot \mathbf{m}) \times (\hat{\mathbf{e}} \cdot \mathbf{m})F^{(2)}, \quad (1)$$

where $\hat{\mathbf{e}}$, $\hat{\mathbf{e}}'$ are the unit vectors corresponding to polarization modes and \mathbf{m} is the direction of the local magnetic moment of the ion.

Each of the three terms in Eq. (1) is a product of an angular dependent factor describing the geometry and an

atomic resonant factor $F^{(i)}(\omega)$ which depends on the radial distribution functions of the core level electron and the valence electrons involved in the resonance.^{3,33} The $F^{(i)}$ are complex numbers, the imaginary part of $F^{(0)}$ is directly proportional to the x-ray absorption (XAS) whereas the imaginary parts of $F^{(1)}$ and $F^{(2)}$ are proportional to the x-ray circular and linear magnetic dichroism (XMCD and XMLD), respectively. At the transition metal $L_{2,3}$ edges the linear dichroism is small when compared to the circular dichroism. However, at the rare earth $M_{4,5}$ edges the linear dichroism can be considerable,³⁴ and we will show that in the case of Gd this gives rise to a clear contribution to the scattering cross section.

Since domains have typical sizes of 50 nm or bigger, most of the scattered intensity occurs at very small scattering angles. It can simply be shown that in the forward scattering limit the $F^{(1)}$ term is mainly sensitive to the magnetization components parallel to the beam while the $F^{(2)}$ term involves transverse components.³² We find that the latter contribution is located in a narrow energy interval, which makes it possible to switch it by slight adjustment of the photon energy, allowing one in a convenient way to disentangle the intensity from the different magnetization components.

The real and imaginary parts of the $F^{(i)}$ are connected by Kramers-Kronig transforms and therefore it is sufficient to measure either one of these parts directly. The real part has been obtained by measuring the energy dependence of the reflectivity³⁵ or the position of the Bragg peaks from multilayers³⁶⁻³⁸ or thin films³⁹ or from measurements of the Faraday⁴⁰⁻⁴² or Voigt effects.^{43,44} The imaginary part can be obtained in a straightforward way from the polarization-dependent absorption spectra.⁴⁵⁻⁵¹ Because of the high absorption cross sections in the soft x-ray range, these are normally measured in the total electron yield mode, which suffers from saturation effects and does not give absolute values. By normalizing electron yield spectra to calculations for the nonresonant absorption coefficients, it is possible to obtain more quantitative values.^{48,51} The more reliable method relies on transmission measurements on thin metallic films deposited on ultrathin transmission electron microscopy support windows. A number of groups have tried this

approach in the soft x-ray range successfully.^{45–48}

We use this method here to obtain high quality data for the full set of optical constants of Gd and $\text{Gd}_{1-x}\text{Fe}_x$ thin films around the Gd $M_{4,5}$ dipole resonance. For completeness we also give our results for the Fe $L_{2,3}$ resonance. The reliability of these optical constants will be demonstrated by comparison of the resulting scattering cross section with the measured scattered intensity of the magnetic stripe lattices in the same samples. In describing the scattered intensity two points of view can be taken:⁴¹ the macroscopic description in terms of a space modulated refractive index, or a description in terms of the atomic scattering amplitude. Here we choose to use the more intuitive approach of the refractive index formalism in explaining the roles of the dichroic attenuation and birefringence in the scattering contrast.

II. EXPERIMENT

$\text{Gd}_{1-x}\text{Fe}_x$ films grown at room temperature are well known to exhibit a perpendicular anisotropy,^{52–54} which is convenient for transmission XMCD experiments. We grew films of 40 nm thickness using electron beam evaporation at 10^{-9} mbar on room temperature substrates that were rotated to ensure film homogeneity and a true perpendicular anisotropy axis. The compositions and thicknesses were calibrated with Rutherford backscattering spectroscopy. The temperature dependence of the magnetization was measured with a vibrating sample magnetometer. In addition, 18-nm-thick pure Gd films were grown, which are paramagnetic at room temperature. In each case, the thicknesses were chosen to give approximately $1/e$ absorption at the Gd M_5 resonance using calculated cross sections from Thole.⁴ As supports we used 100-nm-thick Si_3N_4 windows, which have a transmission of $\sim 95\%$ at the Gd $M_{4,5}$ and $\sim 85\%$ at the Fe $L_{2,3}$ energy. Typical window dimensions were $0.5 \times 0.5 \text{ mm}^2$. The films were capped with a 2 nm Al protection layer in order to prevent oxidation. Atomic force microscopy showed the films to be flat to within 2 nm and free of defects and pinholes.

Transmission experiments were performed during several runs at beamline ID08⁵⁵ at the European Synchrotron Radiation Facility. This beamline is equipped with two *Apple II* undulators, optimized for polarization dependent soft x-ray spectroscopies. The photon energy is tunable between 0.4 and 1.6 keV and the polarization can be controlled such that the x rays are either 100% left/right circularly polarized or vertical/horizontal linearly polarized. The “Dragon” type spherical grating monochromator has a best energy resolution close to $\Delta E/E = 5 \times 10^{-4}$ at 850 eV. For the present experiment at 1200 eV the experimental resolution was estimated to be 0.3 eV. A vertical refocusing mirror focuses the beam to a minimum vertical size of $40 \mu\text{m}$ at the sample position. The horizontal width is typically $800 \mu\text{m}$, determined by a horizontal focusing mirror, which is used for harmonic rejection.

The experimental layout from the refocusing mirror onwards is sketched in Fig. 1. The intensity of the incident beam upstream of the sample was monitored by the photoelectron current from a fine gold-coated Cu grid. A photodi-

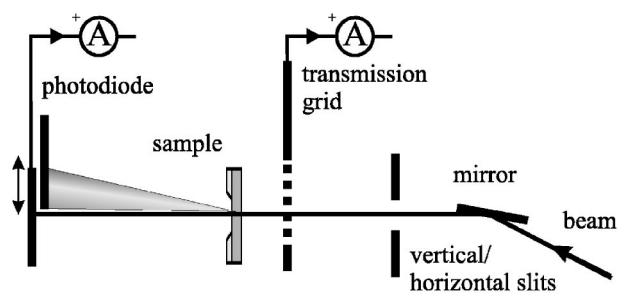


FIG. 1. Schematic experimental layout for the transmission experiment. The photodiode can be translated and intercepts either the scattered intensity as shown or the transmitted intensity direct beam.

ode was used to detect the transmitted intensity. Absolute transmission factors were determined by measuring the ratio of the two detector signals with and without the sample. A set of slits in front of the I_0 monitor was used to produce a beam size smaller than the Si_3N_4 window dimensions.

The samples were attached to a cold finger inserted between the poles of a horizontal 0.5 T in-vacuum electromagnet. The maximum magnetic field was sufficiently high to saturate all samples. For x-ray magnetic circular dichroism (XMCD) measurements the field direction was parallel to the beam. The magnetization was flipped at each data point to obtain the dichroism spectrum, and the measurements were performed for two helicity directions, which gave indistinguishable results. The x-ray magnetic linear dichroism (XMLD) was measured with the sample magnetized perpendicular to the beam, taking the difference of consecutive scans with horizontal or vertical linear polarization.

III. ABSORPTION AND MAGNETIC DICHOISM CROSS SECTIONS

Since for x rays the complex refractive index is close to 1 it is written as

$$n(\omega) \equiv 1 - \delta(\omega) + i\beta(\omega), \quad (2)$$

where $1 - \delta$ and β are related to the dispersion and absorption in the medium, $\beta(\omega)$ is related to the absorption coefficient $\mu(\omega)$ by $\mu(\omega) = 2\beta(\omega)k$ where k is the wave number. In the absence of scattering, i.e., for films that are homogeneous on length scales larger than the wavelength (1 nm), the absorption coefficient $\mu(\omega)$ is equal to the extinction coefficient and is given by the Lambert-Beer law

$$\mu = -1D \ln(I_t / I_0), \quad (3)$$

where I_t and I_0 are the transmitted and incident intensities and D the film thickness. In a magnetic medium the refractive index is only defined for the so-called *proper modes* of polarization⁵⁶ which correspond to the two solutions of the wave equation existing for a given direction of propagation \mathbf{k} of the electric wave and magnetization vector $\hat{\mathbf{m}}$.^{56–59} For propagation along the magnetization direction $\mathbf{k} // \hat{\mathbf{m}}$ it can be shown that these proper modes are left and right circularly polarized plane waves e_{\pm} with refractive index n_{\pm} . For propa-

TABLE I. Scattering cross section for the proper polarization modes for propagation parallel and perpendicular to \mathbf{m} .

\mathbf{m}/\mathbf{k}	$\mathbf{m} \perp \mathbf{k}$
$\hat{\mathbf{e}}_{\pm} = \frac{1}{\sqrt{2}}\sqrt{2}(1, \pm i, 0)$	$\hat{\mathbf{e}}_{//} = (0, 0, 1)$
$f_{+}(\omega) = f^0 + F^{(0)}(\omega) - F^{(1)}(\omega)$	$\hat{\mathbf{e}}_{\perp} = (0, 1, 0)$
$f_{-}(\omega) = f^0 + F^{(0)}(\omega) + F^{(1)}(\omega)$	$f_{//}(\omega) = f^0 + F^{(0)}(\omega) + F^{(2)}(\omega)$
	$f_{\perp}(\omega) = f^0 + F^{(0)}(\omega)$

gation perpendicular to the magnetization $\mathbf{k} \perp \hat{\mathbf{m}}$ the solutions are *linearly* polarized waves, either parallel $\hat{\mathbf{e}}_{//} = \hat{\mathbf{m}}$ or perpendicular $\hat{\mathbf{e}}_{\perp} \perp \mathbf{k} \times \hat{\mathbf{m}}$ to the magnetization with corresponding refractive indices $n_{//}$ and n_{\perp} .

The connection between the refractive index and atomic scattering factors in Eq. (1) follows from the optical theorem which relates the imaginary part f'' of the forward atomic scattering amplitude

$$f(\mathbf{k}' = \mathbf{k}) = f^0 + f'(\omega) + if''(\omega) \quad (4)$$

to the absorption. Here $f^0 = Z$ is the Thomson scattering length for the Z “free” electrons in the atom and f' and f'' are the frequency dependent dispersion and attenuation corrections, respectively. Table I gives the resonant forward scattering amplitudes $f_{r,m}$ for the proper modes $m = \pm, //, \perp$ in terms of the scattering factors $F^{(i)}$ that follow from Eq. (1) by taking $\hat{\mathbf{e}}' = \hat{\mathbf{e}} = \hat{\mathbf{e}}_m$.

The total absorption coefficient μ_m measured for a proper circular (\pm) or linear ($\perp, //$) polarization mode is related to the forward scattering cross section through

$$\mu_m = -\frac{f''_{r,m} 4\pi\rho_r r_0}{k} - \sum_n \frac{f''_n 4\pi\rho_n r_0}{k}, \quad (5)$$

where $f''_{r,m}$ is the imaginary part of the forward resonant scattering amplitudes, ρ_r is the corresponding atomic number density and $-r_0$ is the free electron scattering length. The nonresonant second term f''_n describes the absorption by the Si_3N_4 support, the Al capping layer and the nonresonant Fe or Gd species. They contribute to a magnetization independent background absorption, which can be obtained from tabulated atomic absorption cross section calculations⁶⁰ using the known thickness and atomic number densities ρ_n .

The three measurable spectra are the nonmagnetic XAS spectrum

$$\mu_{\text{unpolarized}} = -\frac{4\pi\rho_r r_0}{k} \text{Im}[F^{(0)}] + \sum_n \frac{f''_n 4\pi\rho_n r_0}{k}, \quad (6)$$

the XMCD spectrum defined as

$$\mu_{+} - \mu_{-} = \frac{4\pi\rho_r r_0}{k} \text{Im}[F^{(1)}] \quad (7)$$

and the XMLD spectrum defined as

$$\mu_{//} - \mu_{\perp} = -\frac{4\pi\rho_r r_0}{k} \text{Im}[F^{(2)}]. \quad (8)$$

After subtraction of the nonresonant background the XAS gives the imaginary part of the resonant charge scattering length $F^{(0)}(\omega)$ while the XMCD is directly proportional to the imaginary part of $F^{(1)}(\omega)$ and the XMLD gives the imaginary part of $F^{(2)}(\omega)$, as follows from Table I and Eqs. (1) and (5).

The transmission at room temperature of a paramagnetic 16 nm Gd sample is shown in Fig. 2. The raw signal shown in the inset has been corrected for the sloping transmission of the 100 nm Si_3N_4 support and the energy dependencies of the detectors. The nonresonant background calculated from the known thickness and tabulated cross sections⁶⁰ is also shown, and gives good agreement with the pre- and postedge regions. Using Lambert-Beer’s law and the known atomic density and thickness, the absolute cross section per atom can be calculated as shown in the top panel of Fig. 3.

Also shown in Fig. 3 are the Gd $M_{4,5}$ XMCD and XMLD spectra of $\text{Gd}_{1-x}\text{Fe}_x$ thin films ($x = 72.5\%$ and 83.3%) taken during different experimental runs at room temperature and 20 K. The obtained Gd atomic cross sections for the different compositions differed less than 2%. The XMCD spectrum at 20 K has a maximum amplitude that is $\sim 90\%$ of the maximum isotropic x-ray absorption, implying a fully saturated $4f$ moment.³⁴ The room temperature XMCD spectra have been scaled up to the 20 K spectra by a multiplication factor of 1.31. Since the XMCD is linearly proportional to the total Gd moment M_{Gd} , this implies that at room temperature M_{Gd}

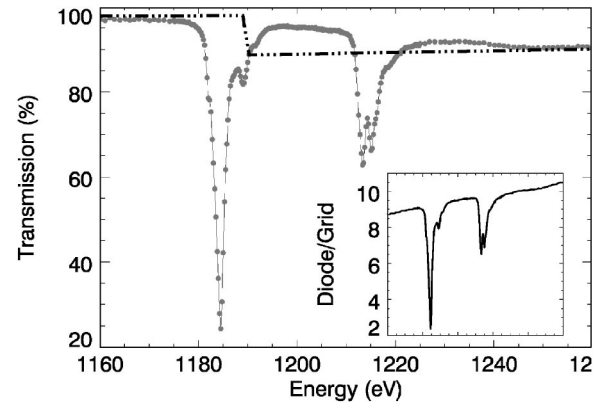


FIG. 2. $M_{4,5}$ transmission spectrum of a 16 nm Gd thin film at room temperature (gray dots). Dash-dotted line: nonresonant contribution. Inset: raw data.

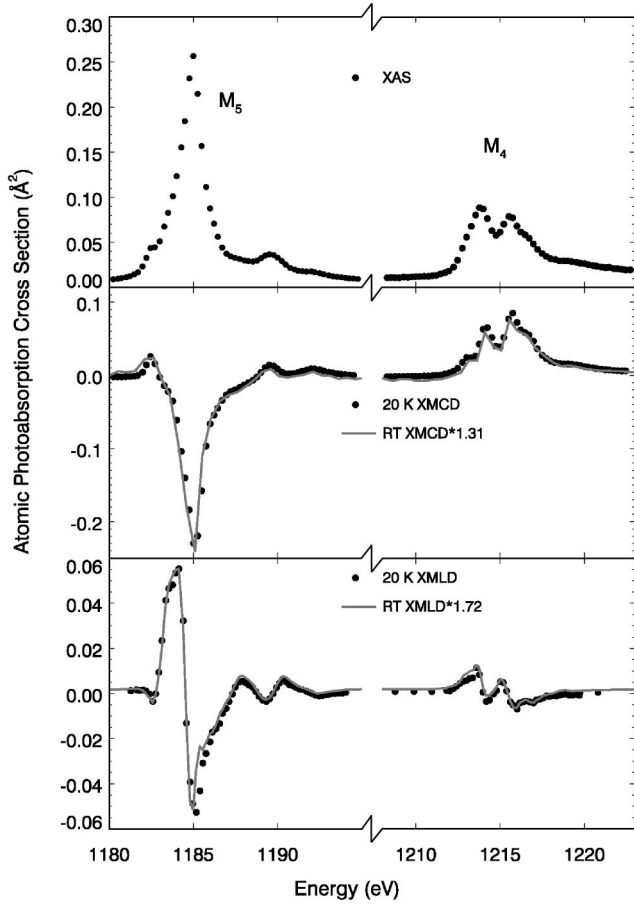


FIG. 3. XAS, XMCD and XMLD spectra at 20 K (symbols) and room temperature (lines). The room temperature spectra are scaled by 1.31 for the XMCD and by 1.31^2 for the XMLD.

is reduced by a factor $1/1.31$ compared to the fully saturated 20 K moment.

Our absorption data are in qualitative agreement with β values derived from electron yield measurements,⁵¹ which were scaled to tabulated literature values⁶⁰ to obtain absolute cross sections. It should be stressed that our values are based purely on experimental results. The appreciably larger XMCD amplitude in our data is either due to a higher magnetic saturation in our sample or to saturation effects⁴ in the total yield data.

The Fe $L_{2,3}$ spectra for the $\text{Gd}_{27.5}\text{Fe}_{72.5}$ magnetic thin film are shown in Fig. 4. In comparison to the Gd $M_{4,5}$ the resonance is weaker. Again, off resonance we obtain very good agreement with the tabulated absorption cross section,⁶⁰ indicated by the dashed line. The linear dichroism at this edge was less than 1% and we were unable to obtain reliable data with the small beam size imposed by the support window dimensions. The much smaller linear dichroism is due to the smaller spin-orbit interaction in the Fe $3d$ shell in comparison with the Gd $4f$ shell.^{61,62}

IV. KRAMERS-KRONIG TRANSFORMATIONS

Based on causality arguments it can be shown that the real and imaginary part of the refractive index, and hence of the

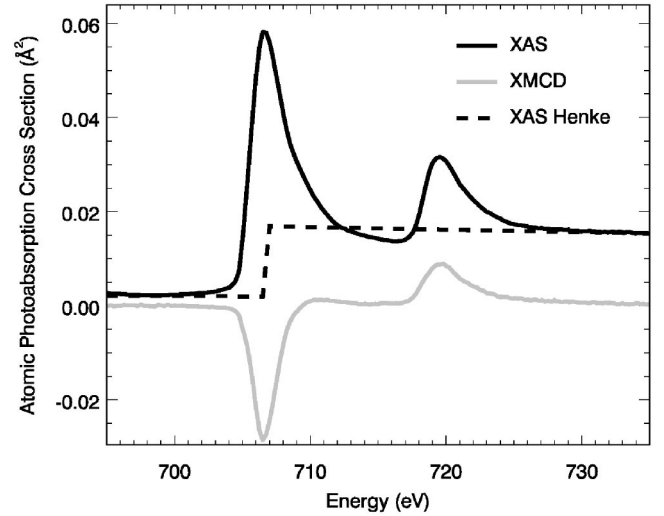


FIG. 4. The Fe $L_{2,3}$ x-ray absorption and circular magnetic dichroism spectra of a 40 nm $\text{Gd}_{27.5}\text{Fe}_{72.5}$ thin film at room temperature. Dash-dotted line: nonresonant contributions from Ref. 60.

atomic scattering factors, are related.⁶³ For the resonant scattering factors $F^{(i)}$ the dispersion relations are^{57,58}

$$\text{Re}[F^{(0)}(\omega)] = \frac{2}{\pi} P \int_0^{\infty} d\omega' \omega' \frac{\text{Im}[F^{(0)}(\omega')]}{\omega'^2 - \omega^2}, \quad (9)$$

$$\text{Re}[F^{(1)}(\omega)] = \frac{2\omega}{\pi} P \int_0^{\infty} d\omega' \frac{\text{Im}[F^{(1)}(\omega')]}{\omega'^2 - \omega^2}, \quad (10)$$

$$\text{Re}[F^{(2)}(\omega)] = \frac{2}{\pi} P \int_0^{\infty} d\omega' \omega' \frac{\text{Im}[F^{(2)}(\omega')]}{\omega'^2 - \omega^2}, \quad (11)$$

where the P stands for the Cauchy principal part of the integral. Note that the role of the frequency in Eq. (10) is slightly different; this is due to the breaking of time-reversal symmetry in the presence of a magnetic field, as pointed out by D.Y. Smith.

These relations allow us to calculate the x-ray dispersion and magnetic birefringence from the experimental absorption and magnetic dichroism spectra. The principal value integrals were approximated numerically by calculating the Riemann sum over the spectra, leaving out the pole at $\omega = \omega'$. The XAS spectrum was combined with tabulated values⁶⁰ to take into account the absorption due to all other transitions from 10 to 30 keV. We enlarged the integration range until no changes in the resonant dispersion were found. For the XMCD and XMLD it suffices to integrate the experimental spectra, from 1150 to 1250 eV, since the magnetic dichroism is negligible away from the sharp $M_{4,5}$ resonance. Other dichroic edges such as the Fe $L_{2,3}$ and Gd $M_{2,3}$ are far away in energy.

Although not directly visible in Fig. 3, the 20 K spectra are noisier and have a slightly sloping background from 1150 to 1250 eV, which hampers the Kramers-Kronig transformation. In the following analysis we therefore used the better quality room temperature XMCD data scaled by the factor

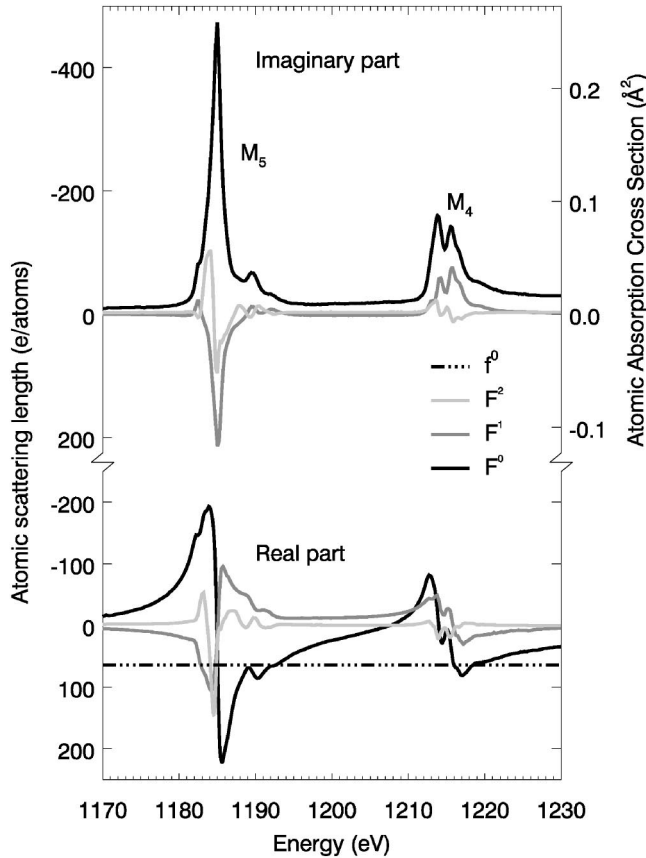


FIG. 5. Resonant amplitudes at the Gd $M_{4,5}$ edges. Shown are the complex charge $F^{(0)}$, circular magnetic $F^{(1)}$, and linear magnetic $F^{(2)}$, atomic scattering factors as function of energy in units of r_0 . top: imaginary parts, from the experimentally determined absorption cross section. Bottom: real part, Kramers-Kronig transform of the imaginary parts. Right axis: approximate atomic cross sections in \AA^2 using a fixed wavelength for $E=1200$ eV. Dash-dotted line: high energy limit of the atomic scattering amplitude $Z=64$.

1.31 for the calculations of the atomic scattering amplitudes. Likewise, for the XMLD spectrum we used the room temperature spectrum multiplied by $1.72=1.31^2$, in excellent agreement with the expectation that the XMLD is proportional to M_{Gd}^2 .

The consistency of the procedure was checked by back transformation of the calculated dispersion and birefringence curves which reproduces the absorption and dichroism spectra with a maximum deviation of $\sim 2\%$ at the extremal values.

The results are presented in Fig. 5 which shows the complex charge $F^{(0)}$, circular magnetic $F^{(1)}$ and linear magnetic $F^{(2)}$ scattering amplitudes in units of the free electron scattering length $-r_0$. The imaginary parts obtained from the transmission experiments are shown at the top, the real parts obtained from the dispersion relation at the bottom. The resonant scattering amplitudes are substantially larger than the constant Thomson scattering amplitude f^0 of 64 electrons, indicated by the dash-dotted line. On the right axis, the atomic absorption cross section corresponding to the imaginary part of the scattering amplitudes is given, for a fixed energy of 1200 eV which results in a $\sim 5\%$ error over this energy range.

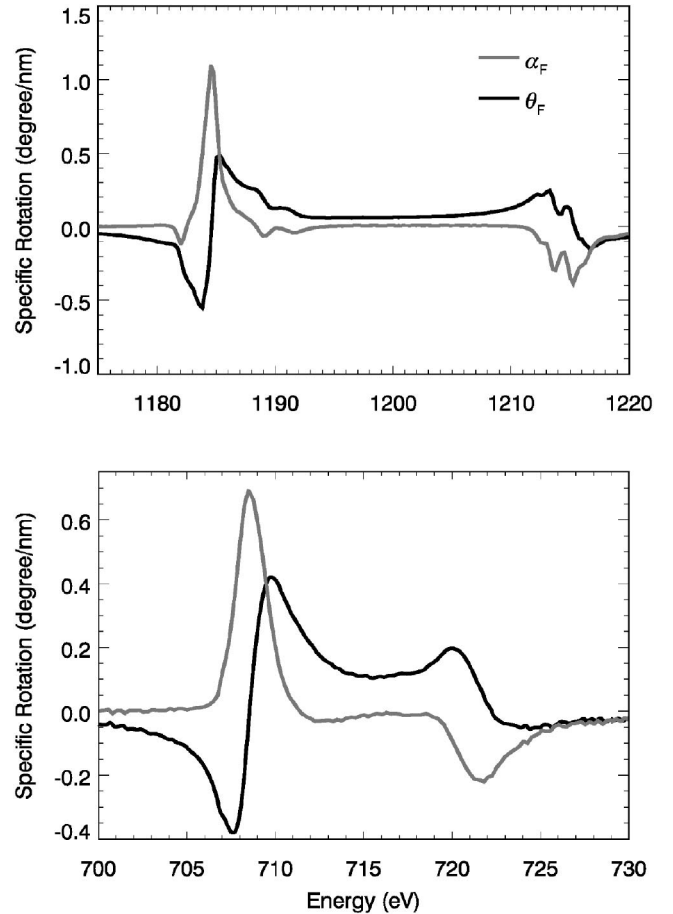


FIG. 6. Specific ellipticity α_F , and rotation angles θ_F of magnetically saturated Gd (top) and Fe (bottom).

The curves in Fig. 5 represent the real and imaginary parts of the atomic scattering factors at the Gd $M_{4,5}$ resonance. Since they have a very large amplitude, they completely determine the magneto-optical properties of the medium.

As an useful application we derive the Faraday rotation and ellipticity angles for both elements. The complex Faraday angle is given by^{41,56}

$$\epsilon_F = \theta_F + i\alpha_F = \frac{n_+ - n_-}{2} kD, \quad (12)$$

where α_F is the ellipticity angle and θ_F is the rotation angle of the linear polarized beam after passing a film of thickness D . From the relation between the forward scattering cross-section and the refractive index⁶⁴ we obtain

$$\Delta n(\omega) = -\frac{2\pi r_0 \rho}{k^2} F^{(1)}(\omega). \quad (13)$$

Although our $F^{(1)}$ data are strictly valid only for Gd and Fe in the GdFe alloy, we use this equation to obtain the specific rotation and ellipticity angles of pure Gd or Fe films. These are given in Fig. 6 as a function of the photon energy, where we have used the atomic densities of pure Gd and Fe. For the Gd edge these curves should be very reliable, due to the chemical insensitivity of the $M_{4,5}$ XAS spectra. The

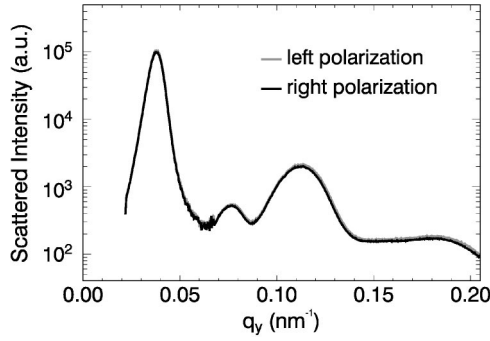


FIG. 7. Diffraction pattern from the aligned stripe domain structure.

maximum rotation angle is $-0.6^\circ/\text{nm}$ and the maximum ellipticity is $1.2^\circ/\text{nm}$, roughly an order of magnitude larger than at optical frequencies. The Fe spectra are more sensitive to alloy formation, and this may explain that, while we have the same line shape, we obtain slightly smaller maximum rotation angles compared to earlier work.⁴¹

It is worth noting that the much higher atomic absorption cross section of Gd is partly compensated by the larger atomic volume, making the difference in optical activity of Gd and Fe much smaller than could be expected.

V. SCATTERING CROSS SECTIONS VERSUS SCATTERED INTENSITY

Magnetic thin films with perpendicular anisotropy can form stripe lattices in which the magnetization is alternately up or down. They result from the competition between the perpendicular magnetic anisotropy with the demagnetizing field.⁶⁵ Our 83.3% sample shows such stripes, which after in-plane saturation form a nearly perfect grating of aligned domains with a period of 160 nm.

In order to test the validity of our $F^{(1)}$ and $F^{(2)}$ spectra we measured the energy dependence of the intensity scattered by this grating. As an example, Fig. 7 shows the diffraction pattern of a normally incident circularly polarized beam at the Gd resonance. It consists of a series of strong odd order peaks alternated with much weaker even order peaks.

In simple terms, this pattern can be explained as follows: the incident light sees either an up or down domain, or a domain wall and obtains a local phase lag and absorption. The near field just after the sample is therefore modulated in phase and amplitude and can be written as an average field, which forms the transmitted beam, plus a modulated field, which produces an interference pattern in the far field.

Describing the out-of-plane magnetization modulation as $m_z(y)$, the Bloch wall magnetization separating them has magnetization $m_x(y)$ and closure domains as $m_y(y)$. Since at remanence the net magnetization along the z direction is zero, the up and down domains are of equal width. A simple Fourier analysis then shows that $m_z(y)$ should have odd order diffraction peaks only. This, however, is in contradiction to what is observed in Fig. 7, which does show even order diffraction peaks, albeit weak compared to the odd orders.

These can simply be understood as arising from the light propagating through the Bloch wall and closure domains (see

Table I). Since these in-plane components have $m_x(y)$, $m_y(y) \perp \mathbf{k}$, they involve only $F^{(2)}$ terms which are sensitive to m_x^2 and m_y^2 (see Ref. 32). These quadratic terms have half the period of the stripe lattice and therefore produce “forbidden” even order peaks. The scattering volume of these in-plane magnetization components is much smaller than that of the up-down domains, explaining the low intensity of these peaks despite the fact that we have shown above that $F^{(1)}$ and $F^{(2)}$ can have similar amplitude.

Ignoring for the moment these weak even orders, we first simplify the analysis by neglecting Bloch walls and closure domains by assuming a modulated magnetization profile, $m_z(y)$, that is periodic in y and constant in x . For a normally incident plane wave, $\mathbf{k} // \mathbf{m} // \hat{\mathbf{z}}$, the refractive index must then be described by the refractive indices $n_{\pm} = 1 - \delta_{\pm} + i\beta_{\pm}$ for the allowed circular polarization modes $\hat{\mathbf{e}}_{\pm}$.

For an incident circular polarized plane wave $E_{0,\sigma}$ with helicity $\sigma = \pm 1$ the refractive index at a position y can be written as

$$n(y) = \bar{n} + \sigma m_z(y) \Delta n \quad (14)$$

with a constant helicity averaged part

$$\bar{n} = \frac{n_+ + n_-}{2} = 1 - \bar{\delta} + i\bar{\beta} \quad (15)$$

and a position dependent magneto-optical part sensitive to the magnetization

$$\Delta n = \frac{n_+ - n_-}{2} = -\Delta\delta + i\Delta\beta. \quad (16)$$

It follows that the transmitted electric field can be written as the product of an average part and a modulated part depending on $m_z(y)$

$$E_{\sigma}(y) = E_0 e^{ikDn} e^{ikD\sigma m_z(y)\Delta n}, \quad (17)$$

where E_0 is the amplitude of the incident plane wave. The factor e^{ikDn} gives rise to an irrelevant phase shift $e^{ikD(1-\bar{\delta})}$ and an absorption $e^{-kD\bar{\beta}}$ equivalent to the helicity averaged attenuation for the uniformly magnetized sample.

The modulated phase and amplitude factor $e^{i\sigma kDm_z(y)\Delta n}$ will scatter light out of the incident direction. The far-field Fraunhofer amplitude is the Fourier transform of Eq. (17)

$$E_{\sigma}(q_y) = E_0 e^{-kD\bar{\beta}} \int e^{ikD\sigma m_z(y)\Delta n} e^{iq_y y} dy, \quad (18)$$

where we have omitted the common phase factor $e^{ikD(1-\bar{\delta})}$ and ignored other prefactors of the Fourier integral that are not important here. Provided $kD\Delta\delta$ and $kD\Delta\beta$ are small, we may expand the argument of the Fourier transform as

$$e^{ikD\sigma m_z(y)\Delta n} \approx 1 + ikD\sigma m_z(y)\Delta n = 1 + i\sigma m_z(y)\epsilon_F \quad (19)$$

and we obtain

$$E_{\sigma}(q_y) = E_0 e^{-kD\bar{\beta}} \int [1 - \sigma m_z(y) kD(i\Delta\delta + \Delta\beta)] e^{iq_y y} dy, \quad (20)$$

where the first term is nonzero only at $q_y=0$ and can be interpreted as the transmitted beam. The scattered field at $q_y \neq 0$ is seen to be proportional to the Fourier transform of the out-of-plane magnetic periodic structure times the frequency dependent magneto-optical constants attenuated by the helicity averaged absorption spectrum.

The far-field Fraunhofer diffraction pattern from the aligned stripe domain lattice consists of a series of diffraction maxima periodically spaced in reciprocal space, as shown in Fig. 7. Here we are interested in the energy dependence of the total scattered intensity $I_s(\omega)$. Integrating $|E_{\sigma}(q_y)|^2$ over q_y , leaving out the direct beam at $q_y=0$, the Fourier transform enters as a constant pre-factor in the energy dependence

$$I_s(\omega) \propto I_0 e^{-2kD\bar{\beta}(\omega)} k^2 D^2 [\Delta\delta(\omega)^2 + \Delta\beta(\omega)^2], \quad (21)$$

$$\propto I_0 e^{-2kD\bar{\beta}(\omega)} \left(\frac{2\pi r_0 D \rho}{k} \right)^2 |F^{(1)}(\omega)|^2, \quad (22)$$

where we have used Eq. (13). This can be rewritten as

$$I_s(\omega)/\bar{I}_t \propto (\omega) \left(\frac{2\pi r_0 D \rho}{k} \right)^2 |F^{(1)}(\omega)|^2, \quad (23)$$

where $\bar{I}_t(\omega) = I_0 e^{-2kD\bar{\beta}(\omega)}$ is the helicity averaged transmission spectrum, which was obtained by having the diode intercept both the transmitted and scattered radiation.

The total scattered intensity $I_s(\omega)$ around the Gd $M_{4,5}$ and the Fe $L_{2,3}$ edges was measured by moving the diode to a position just out of the primary beam where it intercepts only the top half of the diffraction pattern (Fig. 1). The spectrum of $I_s(\omega)/\bar{I}_t(\omega)$ is shown in Fig. 8, and compared to the right hand side of Eq. (23) for the resonant scattering factor $|F^{(1)}(\omega)|^2$ obtained from the measured absorption data and their Kramers-Kronig transformation. For the Gd $M_{4,5}$, shown at the top, a very satisfactory agreement is obtained over four orders of magnitude, which proves again the validity of the Kramers-Kronig transform for the circular dichroic scattering factor $F^{(1)}$. It is worthwhile to point out that at the resonances the scattering contrast is completely absorptive but elsewhere mainly results from the dispersive part of the scattering factor.

A similar analysis can be made for the Fe $L_{2,3}$ edges, with results given in the bottom graph of Fig. 8. Again a good match between measured intensities and calculated cross sections is obtained over several orders of magnitude. It should be noted that the Fe L edge spectrum is much less peaked, and that the scattered intensity is lower than that found at the Gd M edge.

In the above discussion we have neglected the intensity of the weak even order diffraction peaks produced by $F^{(2)}$ scattering in the in-plane magnetization components, i.e., the Bloch wall and closure domain magnetization. Their contribution is small because they occupy only a small fraction of

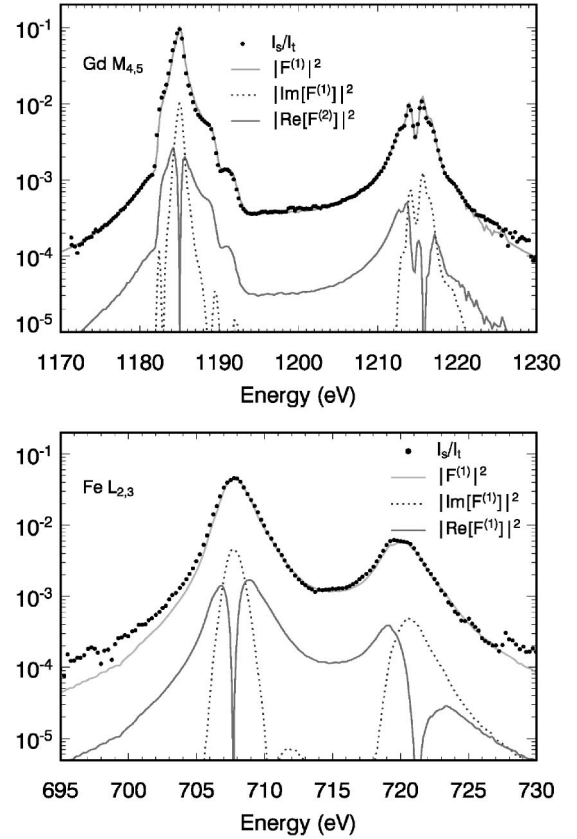


FIG. 8. Magnetic scattering cross section I_s/\bar{I}_t (dots) for an aligned stripe lattice in a 40 nm GdFe₅ thin film compared with the scaled scattering cross section computed from $|F^{(1)}|^2$ (gray lines). Top: Gd $M_{4,5}$ resonance. Bottom: Fe $L_{2,3}$ resonance. The separate contributions from the circular dichroism and birefringence to $|F^{(1)}|^2$ are shown divided by a factor of 10 for clarity.

the total volume. However, from q resolved data as in Fig. 7, taken at remanence ($M=0$) with linear polarization parallel to the Bloch walls, we could isolate the second order intensity using a simple multiple peak fit. Due to the low intensity, meaningful results could be obtained only over a narrow energy range around the M_5 resonance. The results, normalized to the maximum total scattered intensity, are given in Fig. 9. Despite the large error bars, especially below 1182 eV where the scattered intensity decreases rapidly (cf. Fig. 8), it is clear that data points follow the ratio of $|F^{(2)}|^2/|F^{(1)}|^2$ reasonably well, strongly supporting the correctness of the relative size of the $F^{(1)}$ and $F^{(2)}$ scattering amplitudes and in turn the correctness of the Kramers-Kronig transformation of the linear dichroism. The most striking feature of this figure is that at the low energy side of the main absorption peak the linear dichroic contrast term $F^{(2)}$ is nearly as strong as the $F^{(1)}$ term. Hence the linear magnetic scattering term can be switched on or off by changing the energy by only 1 eV.

VI. CONCLUSIONS

In conclusion, we have presented an analysis of the optical constants of prototypical rare earth and transition metal soft x-ray absorption edges. We have measured the polariza-

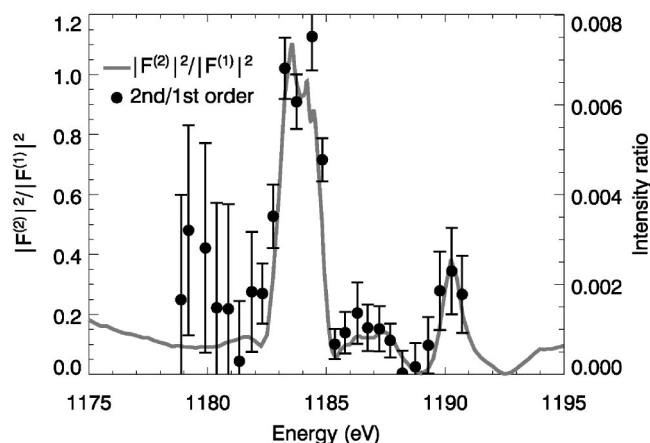


FIG. 9. Full curve/left axis: the ratio of $|F^{(2)}|^2/|F^{(1)}|^2$. Dots/right axis: Ratio of the intensities of the second to first order diffraction peaks as a function of photon energy.

tion and spin dependent transmission spectra of thin $\text{Gd}_{1-x}\text{Fe}_x$ layers at the Gd $M_{4,5}$ and Fe $L_{2,3}$ absorption edges in order to completely determine the optical constants at these edges.

The measured *absolute* absorption cross sections form the imaginary part of the resonant scattering amplitude. The corresponding real part was calculated using Kramers-Kronig relations. Quantitative values for the atomic cross sections for x-ray absorption and magnetic circular and linear dichroism were obtained.

We found that at the Gd $M_{4,5}$ the maximum resonant scattering amplitude is a factor of 10 higher than the nonresonant Thomson scattering length, which is likely to be among the largest resonant enhancements *per atom* that can be found.^{3,34,66,67} The circular dichroism in the scattering cross section is huge, $\sim 90\%$ of the maximum resonant charge contrast, while the linear dichroism, $\sim 30\%$ of the resonant enhancement, is still quite considerable.

We find that the ratio of linear to circular dichroic contributions in the total scattering cross section displays a step-like energy dependence, which can be used to toggle linear dichroic contributions on or off with a negligible change in wavelength and therefore scattering vector. In a forthcoming paper it will be shown that this possibility allows the simultaneous measurement of magnetization components along and perpendicular to the beam direction. The optical constants obtained here were tested by comparing calculated

scattering cross section spectra with the scattered intensity from a quasiperiodic magnetic stripe lattice system. We presented an analysis of this scattering data in terms of a space-modulated refractive index, showing that the scattered intensity can be written as the product of an average isotropic attenuation factor and an anisotropic magnetic scattering contrast. In this description, the agreement between the calculated and measured scattering from the Gd $M_{4,5}$ $F^{(1)}$ contribution is found to be excellent over four orders of magnitude. Similarly good agreement was obtained for the Fe $L_{2,3}$ $F^{(1)}$ term. Furthermore, the existence of the plateau in the $F^{(2)}/F^{(1)}$ ratio at the Gd M edge was experimentally confirmed by a measurement of the first and second order satellite intensity.

The local nature of the Gd $3d \rightarrow 4f$ transition makes it rather insensitive to the chemical surrounding and we expect therefore that the optical constants presented here are applicable for all compounds containing magnetically saturated Gd ions (except for the background absorption). In comparison, the Fe resonant atomic scattering lengths are about a factor of 10 lower in amplitude, with a circular dichroism of 50%. Linear dichroism could not be observed in the GdFe compounds studied here. Since the $L_{2,3}$ edge involves delocalized valence states, the optical constants given here are less universally applicable than those of the Gd $M_{4,5}$ edge, although the magnitude of the cross section away from the absorption edge should be small. Finally, it should be noted that although the atomic scattering amplitudes at the transition metal $L_{2,3}$ edges are lower, the total scattering amplitude at these edges per unit thickness can be comparable to that of rare earth $M_{4,5}$ edges, due to the much smaller atomic radius of the $3d$ transition metals compared to that of rare earth ions.

ACKNOWLEDGMENTS

The work described in this paper was carried out partly at the European Synchrotron Radiation Facility (Grenoble, France) and at the Van der Waals-Zeeman Institute (WZI) of the University of Amsterdam. The work is part of the research program of the Stichting voor Fundamenteel Onderzoek der Materie (FOM) and was made possible by financial support from the Nederlandse Organisatie voor Wetenschappelijk Onderzoek (NWO). We thank Huib Luigjes, the WZI workshop and Kenneth Larsson (ESRF) for their technical support.

*Present address: Philips Medical Systems P. O. Box 10.000 5680 DA Best.

†Present address: Dept. of Chemistry, University of Edinburgh, Joseph Black Building, West Mains Road Edinburgh, EH9 3JJ UK.

‡Present address: IPCMS, 23 rue du Loess, 67037 Strasbourg Cedex, France.

§Electronic address: goedkoop@science.uva.nl

¶Present address: Diamond Light Source, Chilton, Didcot, Oxfordshire, OX11 0QX UK.

¹M. Blume, J. Appl. Phys. **57**, 3615 (1985).

²D. Gibbs, D. Harshman, E. Isaacs, D. McWhan, D. Mills, and C. Vettier, Phys. Rev. Lett. **61**, 1241 (1988).

³J. Hannon, G. Trammell, M. Blume, and D. Gibbs, Phys. Rev. Lett. **61**, 1245 (1988).

⁴B. T. Thole, G. van der Laan, and G. A. Sawatzky, Phys. Rev. Lett. **55**, 2086 (1985).

⁵G. van der Laan, B. T. Thole, G. A. Sawatzky, J. B. Goedkoop, J. C. Fuggle, J. M. Estéva, R. Karnatak, J. P. Remeika, and H. A.

- Dabkowska, Phys. Rev. B **34**, 6529 (1986).
- ⁶G. Schütz, W. Wagner, W. Wilhelm, P. Kienle, R. Zeller, R. Frahm, and G. Materlik, Phys. Rev. Lett. **58**, 737 (1987).
- ⁷G. Schütz, M. Knulle, R. Wienke, W. Wilhelm, W. Wagner, P. Kienle, and R. Frahm, Z. Phys. B: Condens. Matter **73**, 67 (1988).
- ⁸U. Bovensiepen, F. Wilhelm, P. Srivastava, P. Pouloupoulos, M. Farle, A. Ney, and K. Baberschke, Phys. Rev. Lett. **81**, 2368 (1998).
- ⁹J. G. Tobin, G. D. Waddill, and D. P. Pappas, Phys. Rev. Lett. **68**, 3642 (1992).
- ¹⁰B. T. Thole, C. Paolo, F. Sette, and G. van der Laan, Phys. Rev. Lett. **68**, 1943 (1992).
- ¹¹H. Ohldag, A. Scholl, F. Nolting, E. Arenholz, S. Maat, A. T. Young, M. Carey, and J. Stöhr, Phys. Rev. Lett. **91** 017203 (2003).
- ¹²H. Ohldag, A. Scholl, F. Nolting, S. Anders, F. U. Hillebrecht, and J. Stöhr, Phys. Rev. Lett. **86**, 2878 (2001).
- ¹³A. Scholl, J. Stöhr, J. Lüning, J. W. Seo, J. Fompeyrine, H. Siegwart, J. P. Locquet, F. Nolting, S. Anders, and E. E. Fullerton *et al.*, Science **287**, 1014 (2000).
- ¹⁴H. Ohldag, T. J. Regan, J. Stöhr, A. Scholl, F. Nolting, J. Lüning, C. Stamm, S. Anders, and R. L. White, Phys. Rev. Lett. **87** 247201 (2001).
- ¹⁵F. Nolting, A. Scholl, J. Stöhr, J. W. Seo, J. Fompeyrine, H. Siegwart, J. P. Locquet, S. Anders, J. Lüning, and E. E. Fullerton *et al.*, Nature (London) **405**, 767 (2000).
- ¹⁶P. Gambardella, S. Rusponi, M. Veronese, S. S. Dhesi, C. Grazioli, A. Dallmeyer, I. Cabria, R. Zeller, P. H. Dederichs, and K. Kern *et al.*, Science **300**, 1130 (2003).
- ¹⁷P. Gambardella, S. S. Dhesi, S. Gardonio, C. Grazioli, P. Ohresser, and C. Carbone, Phys. Rev. Lett. **88** 047202 (2002).
- ¹⁸J. Stöhr, J. Magn. Magn. Mater. **200**, 470 (1999).
- ¹⁹J. B. Kortright, D. D. Awschalom, J. Stöhr, S. D. Bader, Y. U. Idzerda, S. S. P. Parkin, I. K. Schuller, and H. C. Siegmann, J. Magn. Magn. Mater. **207**, 7 (1999).
- ²⁰E. E. Fullerton, O. Hellwig, K. Takano, and J. B. Kortright, Nucl. Instrum. Methods Phys. Res. B **200**, 202 (2003).
- ²¹P. Gambardella, A. Dallmeyer, K. Maiti, M. C. Malagoli, W. Eberhardt, K. Kern, and C. Carbone, Nature (London) **416**, 301 (2002).
- ²²C. Kao, J. B. Hastings, E. D. Johnson, D. P. Siddons, G. C. Smith, and G. A. Prinz, Phys. Rev. Lett. **65**, 373 (1990).
- ²³C. C. Kao, C. T. Chen, E. D. Johnson, J. B. Hastings, H. J. Lin, G. H. Ho, G. Meigs, J. M. Brot, S. L. Hulbert, and Y. U. Idzerda *et al.*, Phys. Rev. B **50**, 9599 (1994).
- ²⁴J. M. Tonnerre, L. Seve, D. Raoux, G. Soullie, B. Rodmacq, and P. Wolfers, Phys. Rev. Lett. **75**, 740 (1995).
- ²⁵V. Chakarian, Y. U. Idzerda, C. C. Kao, and C. T. Chen, J. Magn. Magn. Mater. **165**, 52 (1997).
- ²⁶H. A. Dürr, E. Dudzik, S. S. Dhesi, J. B. Goedkoop, G. van der Laan, M. Belakhovsky, C. Mocuta, A. Marty, and Y. Samson, Science **284**, 2166 (1999).
- ²⁷J. B. Kortright, S. K. Kim, G. P. Denbeaux, G. Zeltzer, K. Takano, and E. E. Fullerton, Phys. Rev. B **64**, 1 (2001).
- ²⁸J. Stöhr, Y. Wu, B. D. Hermsmeier, M. G. Samant, G. R. Harp, S. Koranda, D. Dunham, and B. P. Tonner, Science **259**, 658 (1994).
- ²⁹P. Fischer, G. Schütz, G. Schmahl, P. Guttmann, and D. Raasch, Z. Phys. B: Condens. Matter **101**, 313 (1996).
- ³⁰O. Hellwig, G. P. Denbeaux, J. B. Kortright, and E. E. Fullerton, Physica B **336**, 136 (2003).
- ³¹E. Dudzik, S. S. Dhesi, S. P. Collins, H. A. Dürr, G. van der Laan, K. Chesnel, M. Belakhovsky, A. Marty, Y. Samson, and J. B. Goedkoop, J. Appl. Phys. **87**, 1 (2000).
- ³²J. P. Hill and D. F. McMorrow, Acta Crystallogr., Sect. A: Found. Crystallogr. **52**, 236 (1996).
- ³³M. Blume and D. Gibbs, Phys. Rev. B **37**, 1779 (1988).
- ³⁴J. B. Goedkoop, J. C. Fuggle, B. T. Thole, G. van der Laan, and G. A. Sawatzky, J. Appl. Phys. **64**, 5595 (1988).
- ³⁵J. M. Tonnerre, L. Sève, A. Barbara-Dechelette, F. Bartolomé, D. Raoux, V. Chakarian, C. C. Kao, H. Fischer, S. Andrieu, and O. Fruchart, J. Appl. Phys. **83**, 6293 (1998).
- ³⁶L. Seve, J. M. Tonnerre, and D. Raoux, J. Appl. Crystallogr. **31**, Part 5, 700 (1998).
- ³⁷M. Sacchi, C. F. Hague, L. Pasquali, A. Mirone, J. M. Mariot, P. Isberg, E. M. Gullikson, and J. H. Underwood, Phys. Rev. Lett. **81**, 1521 (1998).
- ³⁸M. Sacchi and A. Mirone, Phys. Rev. B **57**, 8408 (1998).
- ³⁹R. L. Blake, J. C. Davis, D. E. Graessle, T. H. Burbine, and E. M. Gullikson, in *Resonant Anomalous X-ray Scattering, Theory and Applications*, edited by G. Materlik, C. Sparks, and K. Fischer (Elsevier, New York, 1994), pp. 79–90.
- ⁴⁰J. B. Kortright, M. Rice, and R. Carr, Phys. Rev. B **51**, 10240 (1995).
- ⁴¹J. B. Kortright and K. Sang Koog, Phys. Rev. B **62**, 12216 (2000).
- ⁴²H. C. Mertins, D. Abramssohn, A. Gaupp, F. Schafers, W. Gudat, O. Zaharko, H. Grimmer, and P. M. Oppeneer, Phys. Rev. B **66**, 184404 (2002).
- ⁴³D. Knabben, N. Weber, B. Raab, T. Koop, F. U. Hillebrecht, E. Kisker, and G. Y. Guo, J. Magn. Magn. Mater. **190**, 349 (1998).
- ⁴⁴H. C. Mertins, F. Schafers, A. Gaupp, W. Gudat, J. Kunes, and P. M. Oppeneer, Nucl. Instrum. Methods Phys. Res. A **467**, Part 2 (2001).
- ⁴⁵C. T. Chen, Y. U. Idzerda, H. J. Lin, N. V. Smith, G. Meigs, E. Chaban, G. H. Ho, E. Pellegrin, and F. Sette, Phys. Rev. Lett. **75**, 152 (1995).
- ⁴⁶F. Yubero, S. Turchini, F. C. Vicentin, J. Vogel, and M. Sacchi, Solid State Commun. **93**, 25 (1995).
- ⁴⁷F. C. Vicentin, S. Turchini, F. Yubero, J. Vogel, and M. Sacchi, J. Electron Spectrosc. Relat. Phenom. **74**, 187 (1995).
- ⁴⁸V. Chakarian, Y. U. Idzerda, and C. T. Chen, Phys. Rev. B **57**, 5312 (1998).
- ⁴⁹J. Geissler, E. Goering, M. Justen, F. Weigand, G. Schütz, J. Langer, D. Schmitz, H. Maletta, and R. Mattheis, Phys. Rev. B **65**, 020405 (2002).
- ⁵⁰N. Jaouen, J. M. Tonnerre, D. Raoux, E. Bontempi, L. Ortega, M. Muenzenberg, W. Felsch, A. Rogalev, H. A. Dürr, and E. Dudzik *et al.*, Phys. Rev. B **66**, 134420 (2002).
- ⁵¹J. E. Prieto, F. Heigl, O. Krupin, G. Kaindl, and K. Starke, Phys. Rev. B **68**, 134453 (2003).
- ⁵²Y. Mimura, N. Imamura, and T. Kobayashi, J. Appl. Phys. **47**, 368 (1976).
- ⁵³J. Orehtsky and K. Schröder, J. Appl. Phys. **453**, 2413 (1972).
- ⁵⁴P. Hansen, C. Clausen, G. Much, M. Rosenkranz, and K. Witter, J. Appl. Phys. **66**, 756 (1989).
- ⁵⁵www.esrf.fr/exp_facilities/ID8/ID8.html
- ⁵⁶M. J. Freiser, IEEE Trans. Magn. **4**, 152 (1968).
- ⁵⁷D. Y. Smith, J. Opt. Soc. Am. **66**, 547 (1976).

- ⁵⁸D. Y. Smith, in *Nato Advanced Institute on Theoretical Aspects and New Developments in Magneto-Optics*, edited by J.-T. Devreese (Plenum, Antwerpen, 1979).
- ⁵⁹L. Landau, E. M. Lifshitz, and L. P. Pitaevskii, *Electrodynamics of Continuous Media*, 2nd ed. (Pergamon, New York, 1984).
- ⁶⁰B. L. Henke, E. M. Gullikson, and J. C. Davis, *At. Data Nucl. Data Tables* **54**, 181 (1993).
- ⁶¹M. M. Schwickert, G. Y. Guo, M. A. Tomaz, W. L. O'Brien, and G. R. Harp, *Phys. Rev. B* **58**, R4289 (1998).
- ⁶²S. S. Dhesi, G. van der Laan, and E. Dudzik, *Appl. Phys. Lett.* **80**, 1613 (2002).
- ⁶³R. Kronig and H. A. Kramers, *Z. Phys.* **48**, 174 (1928).
- ⁶⁴J. Jackson, *Classical Electrodynamics*, 3rd ed. (Wiley, New York, 1998).
- ⁶⁵C. Kooy and U. Enz, *Philips Res. Rep.* **15**, 7 (1960).
- ⁶⁶E. D. Isaacs, D. B. McWhan, C. Peters, G. E. Ice, D. P. Siddons, J. B. Hastings, C. Vettier, and O. Vogt, *Phys. Rev. Lett.* **62**, 1671 (1989).
- ⁶⁷C. C. Tang, W. G. Stirling, G. H. Lander, D. Gibbs, W. Herzog, P. Carra, B. T. Thole, K. Mattenberger, and O. Vogt, *Phys. Rev. B* **46**, 5287 (1992).